

Diffusion MRI of the hippocampus

Bradley G. Karat^{1,2}, Stefan Köhler^{1,3}, Ali R. Khan^{1,4}

¹Robarts Research Institute, Schulich School of Medicine and Dentistry, University of Western Ontario, Canada (N6A 3K7), ²Neuroscience Graduate Program, University of Western Ontario, Canada (N6A 3K7), ³Department of Psychology, University of Western Ontario, Canada (N6A 3K7), ⁴Western Institute for Neuroscience, University of Western Ontario, Canada (N6A 3K7)

Conflicts of Interest

The authors declare no competing financial interests.

Acknowledgements

This work was supported in part by funding provided by Brain Canada, in partnership with Health Canada, for the Canadian Open Neuroscience Platform initiative. Bradley G. Karat is supported by a post-graduate scholarship from the Natural Sciences and Engineering Research Council of Canada (NSERC). Ali R. Khan was supported by the Canada Research Chairs program (#950-231964), NSERC Discovery Grant (#6639), and Canada Foundation for Innovation (CFI) John R. Evans Leaders Fund project (#37427), the Canada First Research Excellence Fund, and Brain Canada. Ali R. Khan and Stefan Köhler were supported by a Canadian Institute for Health Research grant (CIHR Project grant #366062). Stefan Köhler is supported by a NSERC discovery grant (#05770).

Abstract

The hippocampus is a brain structure that plays key roles in a variety of cognitive processes. Critically, a wide range of neurological disorders are associated with degeneration of the hippocampal microstructure, defined as neurons, dendrites, glial cells, and more. Thus, the hippocampus is a key target for methods that are sensitive to these micro-scale properties. Diffusion MRI is one such method, which can non-invasively probe neural architecture. Here we review the extensive use of diffusion MRI to capture hippocampal microstructure in both health and disease. The results of these studies indicate that: (i) Diffusion Tensor Imaging is sensitive but not specific to the hippocampal microstructure; (ii) Biophysical modelling of diffusion MRI signals is a promising avenue to capture more specific aspects of the hippocampal microstructure; (iii) Use of ultra-short diffusion times displays unique laminar-specific microstructure contrast and alterations in response to hippocampal injury; (iv) Dispersion of microstructure appears abundant in the hippocampus; and (v) The angular richness of the diffusion MRI signal can be leveraged to improve delineation of the internal hippocampal circuitry. Overall, extant findings suggest that diffusion MRI offers a promising avenue for characterizing hippocampal microstructure.

Introduction

Diffusion MRI as a probe for hippocampal microstructure

Diffusion magnetic resonance imaging (dMRI) is a technique that sensitizes the MRI signal to the diffusion of water (Brown, 1828) which permits the non-invasive analysis of micro-scale properties. In the mammalian brain these micro-scale structures (generally referred to as microstructure) encompass axons, dendrites, and cell bodies (including the glia). Many methods have been developed that aim to extract measures of microstructure via explicit models (such as neurite density), or to quantitatively summarize the diffusion process without making assumptions about the underlying microstructure (see *Diffusion MRI models*). Regardless of the method used, most work conducted with dMRI has focused on characterization and validation of white matter. However, with recent advancements in hardware and software, there has been great interest in leveraging the dMRI signal for characterization of gray matter as well (Palombo et al., 2020; Jelescu et al., 2022).

The hippocampus is a structure in the medial temporal lobe that is largely but not exclusively composed of gray matter. It plays key roles in cognitive processes such as episodic memory formation, consolidation, recollection, and spatial navigation (Voss et al., 2017). The importance of hippocampal structural integrity in these functions is highlighted by the impact hippocampal damage or degeneration can have in many neurological disorders (Small et al., 2011). For example, the well-characterized cell loss of the subiculum and Cornu Ammonis (CA) 1 hippocampal subfields in Alzheimer's disease has been reported to be linked to cognitive deficits (Small et al., 2011). The ability to probe hippocampal microstructure non-invasively can provide valuable insights into its neurotypical cognitive functions and deterioration in diseased states.

In this review we aim to highlight recent advances in research that have applied dMRI in the hippocampus of both human and non-human (primarily rodent) populations. We start by offering an overview of dMRI, including standard modeling techniques. We then discuss the complexity of hippocampal microstructure, providing a background for the kinds of tissue properties that can potentially be captured with dMRI. We then review the current literature, highlighting a wide array of dMRI methods that have been used to study hippocampal microstructure in the neurotypical brain and in neurological diseases. Subsequently, we discuss the relationships between different dMRI measures and histology. We end by summarizing open questions and by suggesting future directions in this research domain.

Diffusion and MRI background

The MRI signal can be sensitized to the diffusion of water by using a particular pulse sequence (i.e. application of varying magnetic gradients). A standard MRI pulse sequence called a spin-echo is depicted in Figure 1A (Jung and Weigel, 2013). A radiofrequency (RF) pulse is applied that “excites” the water molecules, resulting in a measurable signal in nearby receiver coils, where the maximum signal is measured at the echo time (TE; McRobbie et al., 2017). Additional magnetic gradients are introduced to localize the signal in 3D space, which include the slice select gradient (G_s), the phase encode (G_{pe}) gradient, and the frequency encode (G_{fe}) gradient (Figure 1A and B). At the heart of dMRI is the application of multiple magnetic gradients that sensitize the generated MRI signal to the diffusion of water molecules (Figure 1B, blue and red trapezoids or dephasing and rephasing, respectively; Le Bihan, 2010). The three parameters that determine the sensitivity of the MRI signal to diffusion are the gradient strength (G), the time between the leading edges of the gradients (Δ), and the gradient duration (δ) (Figure 1B; Le Bihan, 2010). Figures 1C and D depict how these additional diffusion gradients

work to sensitize the MRI signal to the movement of water. In Figure 1C a dephasing gradient is applied parallel to a cylinder's main axis causing a spatial variation in the frequency of water precession. Precession is the circular movement of the spinning water molecules around a magnetic field (like the peak of a spinning top drawing a circular path as it rotates). That is, the water molecules at the left of the cylinder will precess more slowly, while the water molecules at the right will precess more quickly. Water molecules diffuse more readily parallel to the cylinder's main axis, such that there is a high probability that during the time Δ the molecules are in a different location (Koh and Collins, 2007). The rephasing gradient is then applied, which has equal magnitude and opposite polarity to the dephasing gradient. Since the molecules are not in the same spatial location as when the dephasing gradient was applied, they do not come back into phase via the rephasing gradient, and thus the MRI signal is attenuated. Figure 1D depicts the opposite case where the diffusion gradients are applied perpendicular to the main cylinder axis. The molecules are less likely to diffuse along this direction, and thus the MRI signal is largely recovered. Typical dMRI acquisitions will apply the diffusion gradients across an array of orientations. This leads to the key concept of diffusion MRI: the signal resulting from the application of linear diffusion sensitizing gradients is attenuated in directions of increased molecular diffusion (Le Bihan and Iima, 2015). Thus, dMRI can be used to infer information about the underlying microstructure based on the barriers it poses to water diffusion.

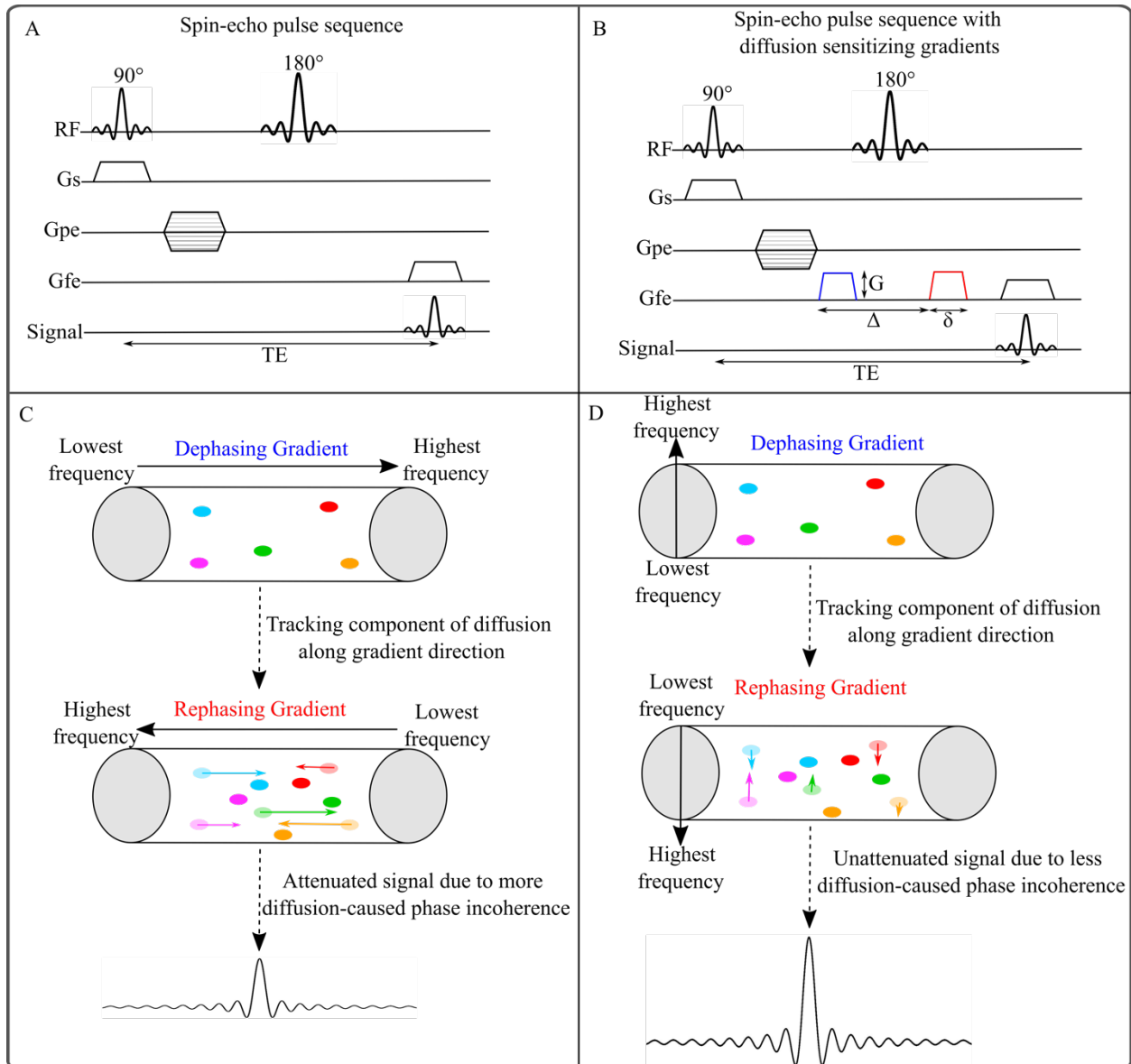


Figure 1. Pulse sequence diagrams and general process of dMRI signal attenuation caused by the addition of diffusion sensitizing gradients. (A) A generic spin-echo pulse sequence diagram with a 90 degree radiofrequency pulse and subsequent 180 degree radiofrequency pulse applied at half of the time to echo. The gray lines within the phase-encoding gradient represent the different strengths of phase encoding applied when reading out the signal. RF-radiofrequency, G_s -Slice select gradient, G_{pe} -Phase encoding gradient, G_{fe} -Frequency encoding gradient, TE-Echo time. (B) The same spin-echo pulse sequence as in (A) with the addition of diffusion-sensitizing

gradients shown in blue and red (Pulsed-Gradient Spin Echo or PGSE sequence). The blue gradient is colloquially referred to as the dephasing gradient, while the red gradient is known as the rephasing gradient. G represents the magnitude or strength of the gradient, Δ is the time between the leading edge of the dephasing and rephasing gradient, and δ is the gradient duration. Note that the dephasing and rephasing gradients are shown in the frequency encoding direction, however, these gradients can be applied in any orientation. (C) A depiction of the diffusion process in a cylinder. Each coloured circle represents one water molecule. Diffusion gradients applied along the main axis of the cylinder results in large signal attenuation due to the large amount of diffusion along this axis. (D) Same example as (C) except the gradient is now applied perpendicular to the main axis of the cylinder. The signal is largely unattenuated as there is minimal diffusion along the probed direction.

Diffusion MRI models

Diffusion MRI models are typically separated into two approaches: signal representations (aka model-free) and biophysical models (aka model-based) (see Figure 2 for an overview). Signal representations are largely based on the statistical properties of water diffusion and make no *a priori* assumptions about the underlying microstructure. While these signal representations are generalizable and well-defined mathematically, they tend to lack microstructural specificity (Jelescu et al., 2017).

The most common signal representation is Diffusion Tensor Imaging (DTI), which characterizes the molecular displacement of water as a 3D Gaussian distribution (Basser et al., 1994). In DTI the diffusion process is represented as a 3x3 matrix (i.e. a tensor), where its eigendecomposition provides useful metrics which describe diffusion. These include the diffusivity along three orthogonal directions (eigenvalues) and the primary orientation of

diffusion (first eigenvector). From this eigendecomposition, metrics such as mean diffusivity (MD - mean of the eigenvalues) and fractional anisotropy (FA - variance of the eigenvalues) can be derived, which have been used extensively to interrogate microstructure. MD characterizes the average measured diffusion along three orthogonal directions, which would be expected to decrease in regions where there is more restriction (i.e. in white matter) and increased in regions where there is less restriction (i.e. cerebrospinal fluid). FA is thought to quantify the degree with which diffusion is preferentially oriented along a particular direction. Put differently, it quantifies how “pointed” the diffusion tensor is. For example, in the cylinder example in Figure 1, diffusion would be preferentially oriented along the cylinder’s main axis, and as a consequence FA would be high. However, the complexity of neural tissue typically results in diffusion that cannot be well described by a single tensor. A common example is given in situations in which two fiber populations are crossing orthogonally to each other, where the measured FA is low while the true underlying anisotropic movement of water is high. Thus, a limitation of DTI is that it conflates orientation dispersion (ex. crossing axons) and anisotropy.

Diffusion Kurtosis Imaging (DKI) also serves as a method for signal representation but aims to estimate the diffusion kurtosis that represents a departure from Gaussian diffusion. The diffusion kurtosis is effectively a measure of heterogeneity of the diffusion environment, suggesting that it has the potential to be more sensitive than DTI to microstructure (Jensen et al., 2005; Jensen & Helpert, 2010). However, since both DTI and DKI do not make explicit distinctions between microstructural environments, their interpretations in terms of specific microstructure is not straightforward (Jensen & Helpert, 2010).

Contrasting with signal representation methods, biophysical models assume a particular geometry of the underlying microstructure, with the goal of extracting the most meaningful

features from the dMRI signal. Mathematical expressions of the diffusion signal are then derived based on the assumed geometry, with the typical assumption that water cannot exchange between these geometrical components (typically referred to as compartments; Jelescu et al., 2020). For example, diffusion in an intra-axonal compartment may be well-represented by the geometry, size, and diffusion properties of a cylinder (Jelescu et al., 2020). While biophysical models can improve microstructure specificity, they can be ill-posed if the assumed geometry is not accurate. Most biophysical models were built for white matter and generally assume that there are two or three compartments in which diffusion is Gaussian. This overarching compartment framework is the so-called standard model of diffusion (Novikov et al., 2018). Neurites and potentially glia processes are represented as impermeable cylinders with zero radius (i.e. “sticks”). Diffusion in the extra-neurite space is described by a diffusion tensor, while a third optional compartment is the cerebrospinal fluid (CSF), which is modeled as a sphere representing completely free diffusion (i.e. no barriers or restrictions). The “sticks” are assumed to be distributed according to an arbitrary orientation distribution function (ODF).

The standard model provides a general framework through which many other biophysical models can be understood. Neurite Orientation Dispersion and Density Imaging (NODDI) is one such biophysical model that assumes three microstructural compartments for water diffusion: intracellular (sticks), extracellular (tensor), and cerebrospinal fluid (sphere) (Figure 2) (Zhang et al., 2012). NODDI captures the primary orientation of diffusion and microstructure dispersion (i.e. the ODF) through a Watson distribution. Commonly derived parameters from NODDI include the Neurite Density Index (similar to the intracellular signal fraction from other biophysical models) and the Orientation Dispersion Index (ODI). The potential gain in specificity of such parameters is clear compared to the signal representations described above,

however, validation remains a challenge (Jelescu et al., 2020). Previous research has found good agreement between NDI and measures of fiber content obtained via electron microscopy (Sepehrband et al., 2015) while another study found no significant association between MRI-derived myelin water fraction and NDI (Qian et al., 2020). As well, conflicting results have been found regarding how well ODI can capture histologically derived fiber dispersion (Schilling et al., 2018; Grussu et al., 2017). Understanding the direct microstructural correlates of parameters derived from biophysical models is a burgeoning area of research.

While modeling gray matter tissue has many parallels to that of white matter, there are generally two distinctions that are made. Firstly, since myelin content is limited in the gray matter, there is the potential for water to exchange across the membrane of the neurites, which implies that the diffusion from each compartment is no longer additive or independent. Secondly, there can be signal contributions from the soma that are not represented in the standard model described above. Tackling the first issue, the Neurite Exchange Imaging (NEXI) model builds upon the standard model by attempting to measure the exchange time between compartments (Jelescu et al., 2022). By contrast, the Soma and Neurite Density Imaging (SANDI) model adds a spherical compartment to account for the presence of the soma, providing measures of soma fraction and radius (Palombo et al., 2020).

To improve characterization of microstructural orientations, Constrained Spherical Deconvolution (CSD) has been proposed to capture orientations through the fiber orientation distribution function (fODF), an alternative to the dODF described above (Tournier et al., 2007). The diffusion signal is assumed to be the convolution of the fODF with the fiber response function, which is the diffusion signal from a single coherent white matter bundle (Tournier et

al., 2007). The shape of the fODF is generally sharper than the dODF and can be used to derive parameters with increased biological saliency like apparent fiber density.

The above-described signal and biophysical models have been designed for single diffusion encoding (SDE) sequences, which probe diffusion along one direction (Figure 1). However, there has been interest in going beyond SDE with double (planar) or triple (spherical) diffusion encoding, which can help disentangle features of various microstructure compartments (like orientation dispersion) within a voxel (Afzali et al., 2022).

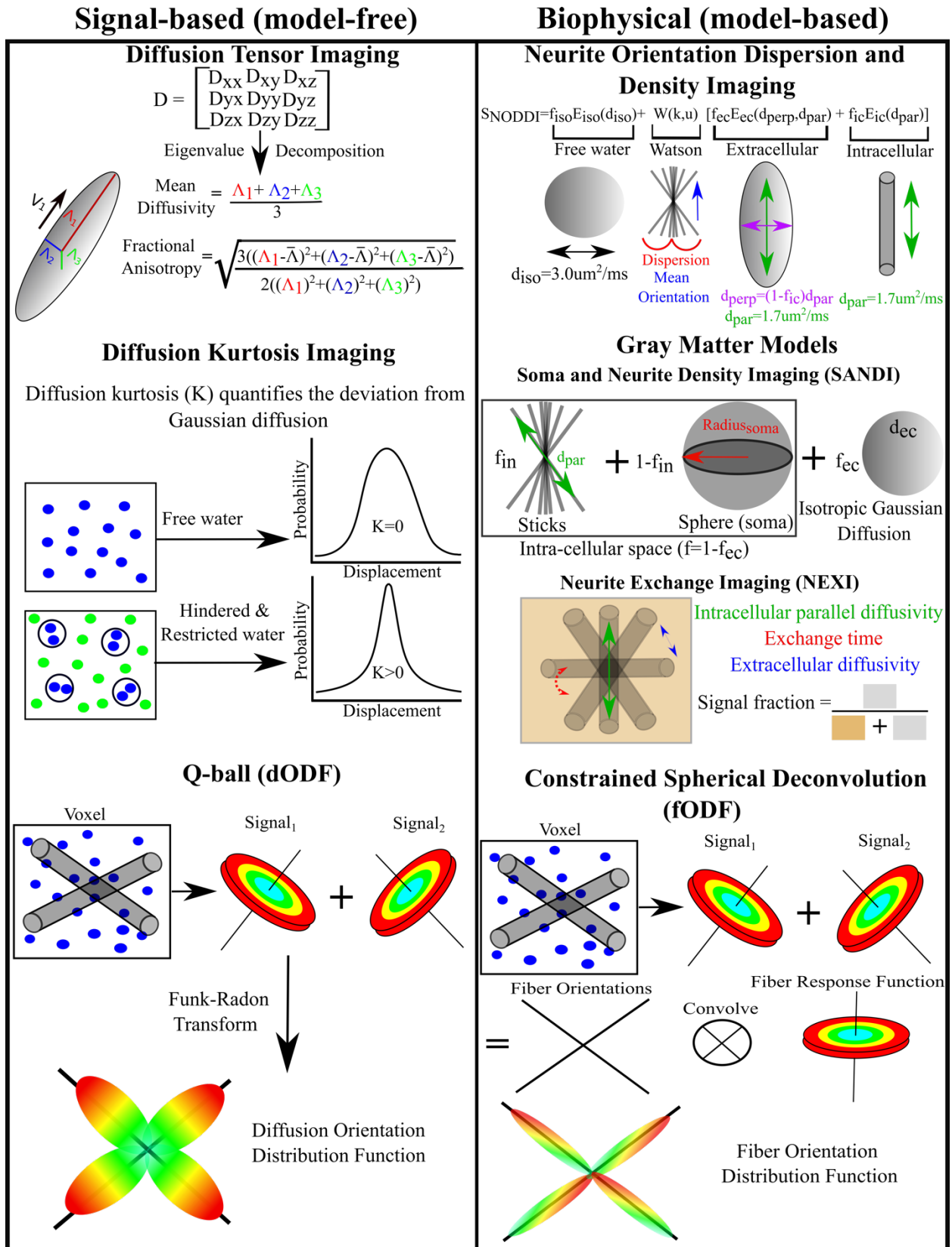


Figure 2. Visual depictions of a variety of dMRI models. Left column shows signal-based

approaches (model-free), including Diffusion Tensor Imaging (DTI) (Basser et al., 1994), Diffusion Kurtosis Imaging (DKI) (Jensen et al., 2005), and the Q-ball method (Tuch, 2004). DTI involves calculation of the diffusion tensor (D). The eigendecomposition of D allows for the calculation of fractional anisotropy and mean diffusivity. DKI quantifies the kurtosis or deviation from Gaussian diffusion, which can be more sensitive to microstructure barriers that restrict the movement of water. The Q-ball method uses the Funk-Radon transform (a spherical integration technique) to obtain the orientation distribution of diffusion that ideally corresponds to the orientation of the underlying microstructure (top left inset under Q-ball section). The right column shows biophysical (model-based) approaches, including Neurite Orientation Dispersion and Density Imaging (NODDI) (Zhang et al., 2012), Soma and Neurite Density Imaging (SANDI) (Palombo et al., 2020), Neurite Exchange Imaging (NEXI) (Jelescu et al., 2022), and Constrained Spherical Deconvolution (CSD) (Tournier et al., 2007). NODDI assumes there are three compartments, where f^* corresponds to the volume fraction of a compartment, d^* corresponds to the diffusivity of a compartment, and E^* is the diffusion signal arising from a compartment. There is a spherical free water compartment (thought to largely correspond to water in CSF), a tensor extracellular compartment, and a “stick” intracellular compartment. The orientation of the extracellular tensor and intracellular “stick” are linked together via a Watson distribution, which captures the orientation distribution with a mean orientation (μ) and dispersion (κ) parameter. The SANDI model adds an additional spherical compartment to capture intra-soma diffusion, with an additional soma radius parameter. The NEXI model drops the spherical soma compartment to measure the exchange time of water more accurately between the intracellular and extracellular space. CSD assumes that the diffusion signal is the convolution

of the fiber (axon bundle) orientations with a fiber response function, which is the signal that arises from a single coherent axon bundle (for example, from the corpus callosum).

Microstructural complexity of the hippocampus

The hippocampus is classically labeled as archicortex due to its distinct 3-layered laminae, in contrast to the 6-layered neocortex (Amaral and Lavenex, 2007). Despite the cell-layer difference, the orientation of hippocampal microstructure resembles that of the neocortex, with notable radial and tangential components as described below (Nieuwenhuys et al., 2008). However, the hippocampus has a unique interlocking “U” shape as it folds inwards. The curvature of the hippocampus is reflected in the complexity of its microstructural components, which are oriented relative to this curvature (Figure 3A and C). Furthermore, the hippocampus is classically divided into meso-scale subfields according to differences in myelo-, cyto-, and chemoarchitecture that define structurally distinct subsections (Amaral and Lavenex, 2007; Nieuwenhuys et al., 2008). These include the subiculum, cornu ammonis (CA) 1-4, and the dentate gyrus. Current work utilizing methods with resolutions on the cellular scale, such as histology and polarized light imaging provides insights into the complexity of the hippocampal microstructural organization. This can then inform consideration of the microstructural properties that dMRI would be sensitive to. In the following sections, we review hippocampal microstructure in the context of subfields, organized based on three broad classes of orientation: radial, tangential, and oblique/anterior-posterior.

Radial hippocampal microstructure

Radially oriented hippocampal microstructure (Figure 3A and C) is defined as aligning with the orientation that crosses the cell layers or put differently, that is oriented orthogonal to the main hippocampal curvature. Generally, radial microstructure stays within the subfields.

Within the hippocampus the dominant radial structure is composed of the pyramidal neurites (Figure 3B and C), which include somas in the stratum pyramidale layer, axonal projections, basal dendrites, and large apical dendrites that project towards the stratum moleculare. Notably, the microstructure of the stratum pyramidale has distinct transitions across the subfields, including changes to the density and shape of the somas (Figure 3C, Williams et al., 2023; Ding and Van Hoesen, 2015). The wide pyramidal layer of the subiculum contains large triangular and globular shaped somas, which tend to be more sparsely packed than CA1 (Rosene and Van Hoesen, 1987; Williams et al., 2023). The large stratum pyramidale layer of CA1 includes somas that are largely triangular, relatively small, and scattered with thin axons (Duvernoy, 2005; Williams et al., 2023; Ding and Van Hoesen, 2015). The narrow stratum pyramidale layer of CA2 contains large and oval shaped somas that are densely packed (Duvernoy, 2005; Williams et al., 2023; Ding and Van Hoesen, 2015). The curved CA3 stratum pyramidale layer contains somas with a similar shape and slightly less packing density than CA2 (Williams et al., 2023; Ding and Van Hoesen, 2015; Insausti and Amaral, 2004). However, a unique feature of CA3 is the presence of unmyelinated mossy fibers (Figure 3C) (Duvernoy, 2005). CA4 is oriented within the concavity of the DG, with large, very sparse, and oval shaped somas intertwined with partly myelinated mossy fibers (Williams et al., 2023; Duvernoy, 2005). Finally, the densely packed somas of the granular neurons in the DG are characteristically small and round.

The axons of the pyramidal cells project through the stratum oriens into the alveus, where they become a part of the fimbria and subsequently of the fornix, forming a large hippocampal white matter efferent (Saunders and Aggleton, 2007; Duvernoy, 2005). The basal dendrites of the pyramidal neurons make short local connections typically bending into the stratum oriens and alveus (Duvernoy, 2005). The large apical dendrites project towards the stratum moleculare

(Figure 3B). The stratum moleculare layer contains few neurons and interneurons, and it contains the arborizations of pyramidal neuron apical dendrites (Figure 3B) (Duvernoy, 2005).

Projections from the entorhinal cortex, which form the perforant path, enter the subiculum in a radial fashion before taking on a more complex curved orientation (Figure 3C) (Zeineh et al., 2017; Duvernoy, 2005). Finally, the majority of hippocampal interneurons appear to be radially oriented, although their components can adopt more complex orientations (Nieuwenhuys et al., 2008).

Tangential hippocampal microstructure

Tangentially oriented hippocampal microstructure (Figure 3A and C) follows the curvature of the hippocampus, that is, it projects across the subfields. The perforant path is one of the major inputs to the hippocampus. Once perforating the subiculum (as mentioned in the section on radial microstructure), the perforant path has a tortuous trajectory, allowing it to project to the granule cells of the dentate gyrus (DG) and the apical dendrites of the Cornu Ammonis fields (Duvernoy, 2005). Importantly, a large part of this trajectory is thought to adopt a tangential orientation (Zeineh et al., 2017). Tangential projections from the dentate granule cells reach the pyramid cells of CA3 as either mossy fibers in the stratum radiatum or as the endfolial pathway in the stratum oriens (Zeineh et al., 2017) (Figure 3C). A large branch of the axons from the CA3 pyramidal cells project to the alveus. At the level of the stratum oriens coarse collaterals are derived from the axons that project to the stratum lacunosum or the stratum oriens in CA1 (Nieuwenhuys et al., 2008). These collaterals are collectively known as the Schaffer collaterals, which largely project tangentially to the hippocampal surface. In turn, the CA1 pyramidal cells have projections to the apical dendrites of the subiculum (Nieuwenhuys et al., 2008). Finally, the subiculum and its constituents project back to the entorhinal cortex. This

closes what is described above as a largely tangentially oriented pathway that is known as the trisynaptic circuit in the broader hippocampal literature.

Anterior-Posterior and other hippocampal microstructure

While we have primarily focused on the radial and tangential hippocampal microstructure, there are aspects that are oriented along the anterior-posterior axis or that do not have a preferred orientation. A major anterior-posterior bundle is the fimbria, which sits atop of CA3, CA4, and the DG (Figure 3C; Zeineh et al., 2017). The thin fibers of the largely tangential but slightly anterior-posterior alveus converge to constitute the fimbria (Nieuwenhuys et al., 2008; Zeineh et al., 2017). At the posterosuperior tail of the hippocampus, the fibers of the fimbria enter the fornix, one of the major fiber systems that connect the hippocampus to other cortical and subcortical areas. It is pertinent to note that while the information-carrying microstructure (i.e. the neurites and fiber pathways) are of great interest, other important micro-scale structures such as oligodendrocytes, astrocytes, microglia, and more can contribute to the diffusion MRI signal. Most of these properties tend to not have a preferred orientation and may have components that extend in many directions. The abundance of these structures greatly increases the micro-scale complexity of the hippocampus, which is discussed in the Concluding Remarks and Future Directions section.

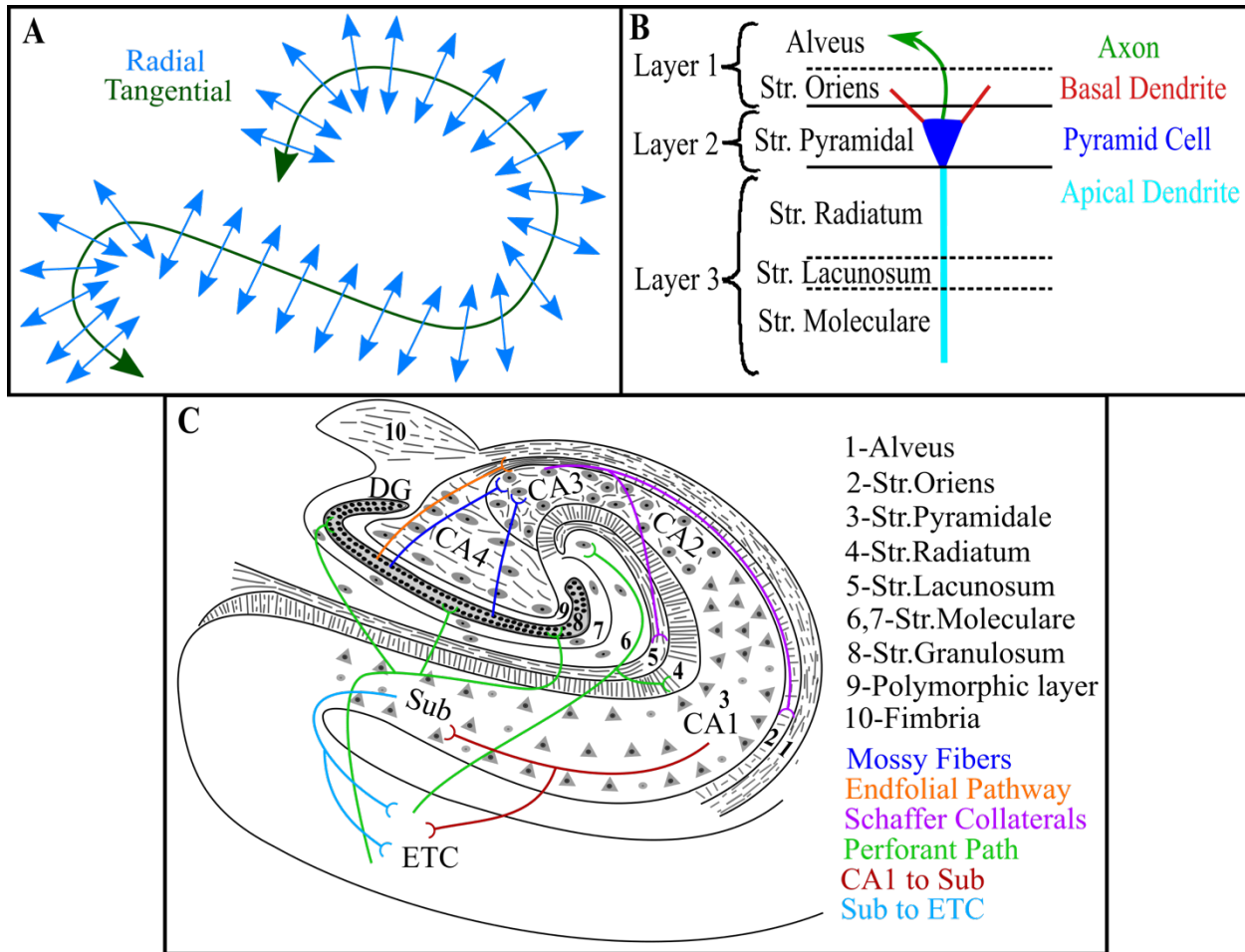


Figure 3. Orientations of hippocampal microstructure on a cartoon coronal section through the hippocampal body (top right of panel C). (A) Radial and tangential directions of the hippocampus. (B) Quintessential hippocampal cell layers representing properties of pyramid cells (Nieuwenhuys et al., 2008). (C) Cartoon depiction of the stereotyped microstructure across the laminar dimension (radial) and across the hippocampal subfields (tangential). Coloured lines and labels represent known microstructural circuits of the hippocampus and their approximate trajectories (Duvernoy, 2005; Nieuwenhuys et al., 2008). CA - Cornu Ammonis, Sub - Subiculum, ETC - Entorhinal cortex, DG - Dentate Gyrus.

Modeling and interpreting the diffusion MRI signal within the hippocampus

In this section we highlight contemporary research that has used dMRI to examine microstructure within the hippocampus. We organize this work based on whether it involved Diffusion Tensor Imaging (DTI) or other types of diffusion-based protocols. Details of the studies reviewed here including scanning protocols, study samples, and analysis types can be found in Table 1.

DTI metrics of FA and MD are sensitive but not specific to the microstructure of the hippocampal laminae

A large volume of studies have modeled the diffusion MRI signal within the hippocampus using Diffusion Tensor Imaging (DTI) (Basser et al., 1994) (see *Diffusion MRI models*). DTI-derived fractional anisotropy and mean diffusivity (FA and MD) have been two popular metrics to quantify diffusion at the voxel level. Both FA and MD have shown good contrast across the hippocampal laminae *ex vivo*, suggesting that both metrics may be sensitive to its underlying microstructural composition (Coras et al., 2014; Shepherd et al., 2006, 2007; Stolp et al., 2018) (Figure 4). FA was shown to provide noticeable differentiation of the alveus, stratum pyramidale, stratum lacunosum moleculare, and the dentate gyrus (DG) molecular layer *ex vivo* (Coras et al., 2014; Shepherd et al., 2007) (Figure 3B; Figure 4A and D).

Correspondingly, MD was found to have an opposite contrast to FA, with MD being lower in regions dominated by axon architectures (fimbria and alveus) and higher in layers of neural soma and neuropil (stratum granulosum, stratum pyramidale, hilus, stratum moleculare and stratum radiatum) (Shepherd et al., 2006, 2007). In contrast to the above studies, it was found that MD could differentiate two cell dense (CA1 pyramidale and DG granular layer) from two cell sparse but projection heavy (CA1 stratum radiatum and DG molecular layer) laminae, while there was

no significant differences in FA (Stolp et al., 2018). The lack of sensitivity of FA to these laminae is likely a result of the high orientational heterogeneity of the hippocampal microstructure (Yoo et al., 2021). Interestingly, it has been shown that the DTI model most accurately captures the diffusion signal in areas of lightly-myelinated axons, such as in the stratum radiatum moleculare (Jespersen et al., 2010). At high *ex vivo* resolutions (50-200 μ m; Table 1) FA and MD generally appear to be useful in contrasting the hippocampal laminae, from highly myelinated axonal regions to the less restrictive neuropil, to the perikarya.

An improved understanding of hippocampal microstructure as seen through the lens of FA and MD has come through studying diseased states, in which known microstructural changes occur. In a rat model of epileptogenesis, FA was found to increase over time in the hilus and DG regions, suggesting that it may be useful in capturing the axonal plasticity of the mossy fibers after epileptic injury (Sierra et al., 2015; Laitinen et al., 2010). Similarly, a major microstructural hallmark of mesial temporal lobe epilepsy (TLE) is hippocampal sclerosis, defined by a loss of pyramidal neurons, reactive gliosis, and morphological changes of the DG. Probing sclerotic hippocampi *ex vivo*, it was found that FA was not sensitive to microstructural changes such as cell death and expanding extracellular space (Coras et al., 2014). MD was increased in the stratum pyramidale of sclerotic hippocampi versus controls, suggesting that it is likely sensitive to changes to the pyramidal somas (Coras et al., 2014; Shepherd et al., 2006, 2007; Stolp et al., 2018). In humans with TLE it was found that MD elevations were regionally heterogeneous within the hippocampus, and this heterogeneity varied across TLE patients; these types of findings suggest that the measure may be capturing region-specific microstructural changes (Treit et al., 2019). In a group of Alzheimer's disease (AD) patients, MD was found to reflect aspects of the neurodegenerative process, with significant changes in the anterior head of the

hippocampus, potentially reflecting perforant path disruption (Fellgiebel and Yakushev, 2011). In another study at ultra-high *ex vivo* resolutions, however, no significant changes in FA or MD were found within the layers of the DG between AD and control tissue (Shih et al., 2023). While non-significant, a decreasing trend in MD was found for AD tissue, which seemingly contradicts previous research in which known hippocampal microstructural degradation increased MD (Coras et al., 2014; Shih et al., 2023; Stolp et al., 2018; Treit et al., 2019). The authors proposed that DTI measures are likely sensitive to many different barriers that hinder water movement, including axonal swelling, accumulation of intracellular NFT, amyloid plaque deposition, and microvascular changes (Shih et al., 2023). In summary, the DTI-based scalar metrics appear to have only limited value in capturing hippocampal circuitry and laminar microstructure. The lack of specificity to any particular cellular organization and inability to represent complex microstructure configurations limits their use in drawing conclusions about any specific microstructural property (Beaujoin et al., 2018). The general limitations of DTI, including those mentioned here, have been extensively acknowledged (Mori and Zhang, 2006).

Biophysical modeling is a promising avenue for improving characterization of hippocampal microstructure

Due to the known shortcomings of DTI, there have been several diffusion-based studies employing increasingly complex signal representations like Diffusion Kurtosis Imaging (DKI) (Jensen et al., 2005) and biophysical models to improve tissue specificity. A popular dMRI biophysical model is the Neurite Orientation Dispersion and Density Imaging (NODDI; Figure 2) model, which provides metrics of orientation dispersion and intracellular volume (Zhang et al., 2012). At high *ex vivo* resolutions, the intracellular volume fraction was shown to provide excellent contrast (i.e., sensitivity) to the hippocampal laminae (Beaujoin et al., 2018) (Figure

4B). Furthermore, heterogeneity in the intracellular volume fraction was seen along the anterior-posterior axis, supporting the idea of hippocampal long-axis differentiation (Beaujoin et al., 2018). Another study using NODDI and surface-based hippocampal modeling *in vivo* found the intracellular volume fraction was significantly correlated with a proxy measure for myelin content (Karat et al., 2023). Furthermore, the subfields were found to be highly separable based on measures of orientation dispersion and intracellular volume fraction, suggesting that these biophysical measures may be sensitive to subfield variability in cyto- and myeloarchitecture (Karat et al., 2023). Further biophysical models were developed to describe diffusion in gray matter (Jespersen et al., 2010). By applying these models in rats, it was found that the cylinder density parameter to capture neurites was very low in the stratum radiatum, which contains non-myelinated axons and dendrites (Jespersen et al., 2010). Due to the short exchange time of water between dendrites and glia to the extracellular space, it is likely that the cylinder density parameter reflected myelinated axons. It was found that these two models describe the diffusion signal better when compared to DTI (Jespersen et al., 2010). Similarly, a more detailed biophysical model was built for diffusion in gray matter, with the goal of characterizing astrocytes and microglia (Garcia-Hernandez et al., 2022). It was found that the parameters prescribed to the microglia and astrocytes were sensitive only to their corresponding activation (Garcia-Hernandez et al., 2022). However, the microglia stick fraction was sensitive to myelin, which is corroborated by (Jespersen et al., 2010). Thus, biophysical modeling is a promising avenue for providing more complete descriptions of hippocampal microstructure, including laminar differentiation, myelinated fibers such as the perforant path, and the abundant glial cells.

A handful of techniques other than DTI and biophysical models have been applied in the hippocampus. Apparent Fiber Density (AFD) derived from Constrained Spherical Deconvolution

(CSD) (Tournier et al., 2007) (Figure 2) was shown to provide better delineation than DTI of the CA1 pyramidal layer and DG granular layer as cell-dense regions versus the CA1 stratum radiatum and DG molecular layer as cell-sparse but projection-heavy layers (Stolp et al., 2018).

Acquisitions with ultra-short diffusion times have shown significant sensitivity to hippocampal microstructure injury

Using oscillating-gradients has allowed for dMRI acquisitions of ultra-short diffusion times, altering the sensitivity of the diffusion signal to local tissue microenvironments. Examining the change in apparent diffusion coefficients (ADC) across varying diffusion times using Oscillating Gradient Spin Echo (OGSE) sequences has shown unique laminar-specific contrasts in the mouse hippocampus (Aggarwal et al., 2013). Furthermore, in response to hippocampal injury, a significant decrease in the change in ADC across diffusion times was found to be specific to the pyramidal and granule cell layers in OGSE based work (Aggarwal et al., 2013). Similarly, an OGSE and standard PGSE sequence has been employed to model the diffusion kurtosis in injured and control mouse brains (Wu et al., 2018). The change in measured kurtosis (ΔM_k) between the two sequences was readily visible in the hippocampus, which may reflect a difference in the scales of the microstructure that is restricting water diffusion (Wu et al., 2018). For example, the 10 μ m radius of the mouse pyramidal neurons is commensurate with the mean displacement of water molecules at the diffusion times of the OGSE sequence, but shorter than the scales probed by the PGSE sequence (Wu et al., 2018).

Microstructural orientation dispersion is likely abundant in the hippocampus

Moving from standard linear tensor encoding (LTE) to spherical tensor encoding (STE) has allowed for the characterization of microscopic fraction anisotropy (uFA), which can help disentangle anisotropy within microscopic compartments from variability in size and orientation

dispersion. Using STE and LTE in humans, uFA has been found to be much higher than FA, suggesting there is substantial orientation dispersion in hippocampal gray matter in which crossing fibers are abundant (Yoo et al., 2021) (Figure 3C).

The angular richness of the dMRI signal can provide distinct hippocampal microstructural orientations

Along with dMRI quantitative modeling, there has been a plethora of research and models that have capitalized on the angular richness of the dMRI signal. Distinct microstructural orientations have been found within the hippocampus by examining the primary eigenvector from DTI (V1; Figure 2). At high *ex vivo* resolutions, the stratum oriens of CA1 and CA3, along with the alveus, have a tangential V1 orientation that is likely a result of axonal projections from the pyramidal neurons bending into the alveus (Shepherd et al., 2007) (Figure 3B and C; Figure 4D). Radial V1 orientations were found within the stratum pyramidale and radiatum, which is thought to represent the large apical dendrites from the pyramidal cells (Shepherd et al., 2006, 2007) (Figure 3B and C; Figure 4D). Similarly, the molecular layer of the DG showed considerable radial orientations, likely resulting from the projections of granule cell dendrites (Shepherd et al., 2007) (Figure 4D). Orientations in the stratum lacunosum moleculare are less distinct than the other regions, which may be due to large amounts of orientational heterogeneity (Shepherd et al., 2007) (Figure 3B and C; Figure 4D). Coinciding with the previous result, within CA1 a radial V1 orientation was found within the stratum pyramidale, while a tangential orientation was found within the alveus (Khan et al., 2015) (Figure 4C). By inducing epilepsy in rats, it was shown that after 10 days the orientation of V1 was altered, suggesting that it is sensitive to underlying hippocampal microstructural changes (Sierra et al., 2015). Using the mean orientation of the Watson distribution provided by NODDI (which is analogous to V1), it

was found that diffusion measured *in vivo* tended to be oriented along the radial, tangential, or anterior-posterior axes, potentially capturing the known stereotyped organization of the hippocampal microstructure (Karat et al., 2023) (Figure 3). However, due to the complex arrangement of hippocampal microstructure, the full diffusion tensor ellipsoid has been shown to be largely spherical, limiting the use of V1 in capturing distinct microstructural orientations, in particular in regions of high orientational heterogeneity (Jespersen et al., 2010; Laitinen et al., 2010). Thus, a handful of studies have gone beyond DTI and used models that can provide accurate orientations even in such regions. The biophysical model developed in Jespersen et al. (2010) appears to capture the more complex arrangement of hippocampal microstructure. Two clear crossing fiber populations thought to represent the radial pyramidal neurites and Schaffer collaterals were found at the level of CA3 using the Q-ball method (Beaujoin et al., 2018; Tuch, 2004) (Figure 2). Similarly, clear shifts in microstructural orientation across the laminae were found using CSD (Stolp et al., 2018; Wu and Zhang, 2016) (Figure 2; Figure 4G). Overall, these studies demonstrate the utility of dMRI orientation estimates for specification and delineation of hippocampal microstructural properties.

By leveraging the dMRI orientations, it is possible to estimate continuous structural connections across extended space. This process is often referred to as tractography and involves propagation of connections (called streamlines) in consecutive steps by following peaks in the estimated orientations. It is a particularly useful technique when attempting to capture intra-hippocampal circuitry non-invasively. Clear streamline orientation shifts were found between laminae in humans and mice by using both DTI and CSD to perform tractography (Ly et al., 2020; Wu and Zhang, 2016) (Figure 4H). Similarly, orientations from DTI, CSD, and Q-ball tractography appeared to show approximate trajectories that may reflect the perforant path,

Schaffer collaterals, mossy fibers, and other components of the trisynaptic and monosynaptic intrinsic hippocampal pathways (Augustinack et al., 2010; Beaujoin et al., 2018; Ly et al., 2020; Modo et al., 2015; Shepherd et al., 2006; Zeineh et al., 2012) (Figure 3C). Tractography has also been applied to the hippocampus in disease states. Streamline differences were found when comparing a sclerotic and non-sclerotic hippocampus in TLE, suggesting a potential shift in the underlying microstructural orientations and larger scale intra-hippocampal circuitry (Coras et al., 2014) (Figure 4E). A similar comparison of streamlines between an AD- and control hippocampus showed distinct regions of disconnectivity and orientation shifts (Shih et al., 2023). It should be noted that some previous studies have used anisotropic voxel resolution for performing tractography, which can be limiting given the potential for preferential averaging of orientations along a given axis (Jones and Leemans, 2010). This can potentially bias measured connectivity between two subfields. Regardless, tractography appears to be a promising technique to elucidate the intricate 3D structure of hippocampal microcircuitry (Figure 3C).

DTI metrics correlate with many histological properties of the hippocampus

While the previously mentioned methods may be useful to model hippocampal microstructure in healthy and diseased states, the relationships of resulting measures to the underlying ground-truth microstructure still remain poorly understood at present. As such, a wide array of histological and optical imaging methods have been employed in combination with dMRI so as to better understand the sensitivity and specificity of the latter to hippocampal microstructure. Beginning with DTI, a positive correlation between histological staining of myelin and FA was found, with both FA and myelin content being high in the alveus and fimbria, and low in the neuropil and pyramidal cell layers (Coras et al., 2014; Laitinen et al., 2010) (Figure 4A). However, FA has also been found to be elevated in regions of high astrocyte

density (Stolp et al., 2018). In a rat model of epilepsy, FA was shown to be increased over time in the hilus and DG regions, while histology revealed a loss of pyramidal cells, gliosis, and activated astrocytes, making it unclear what microstructural changes the FA measure might be sensitive to (Sierra et al., 2015). Similarly, MD was shown to have high spatial correspondence with histological markers of neuronal cell density and gliosis in temporal lobe epilepsy (Treit et al., 2019). Within the granular and pyramidal cell layers, MD was found to be correlated with general cell staining and glia (Stolp et al., 2018). Furthermore, V1 orientation was found to change across laminae when the microstructural composition changed, as shown by a general cell stain, a neuron cell stain, and a glial cell stain (Ly et al., 2020) (Figure 4H). Within a small slice of CA1 and the alveus, it was shown that V1 matches the orientations uncovered with light microscopy stained for Dil (non-specific membrane labeling), suggesting that ultra-high-resolution DTI may be able to capture the general orientation of the ensemble microstructure (Khan et al., 2015) (Figure 4C). Conversely, using a more specific Golgi stain to label hippocampal dendritic arborizations, it was found at lower resolutions that the DTI ellipsoids were generally spherical and not able to capture the true orientation complexity of the dendrites (Jespersen et al., 2010). Overall, DTI-derived measures tend to correlate with many tissue properties but converging evidence for specificity in these mappings remains limited.

Metrics of dMRI other than DTI correlate with more specific aspects of hippocampal microstructure

Moving beyond DTI, it was found that within the stratum radiatum there was a distinct radial orientation of the fODF calculated using CSD (Figure 2), which was reflected in histological staining of axons, astrocytes, and blood vessels (Stolp et al., 2018).

Counterintuitively, AFD was negatively correlated with the staining of axons (Stolp et al., 2018).

The fODF was further shown to have regions of noticeable correspondence with axon and dendrite staining, suggesting that it can capture the basic organization of the hippocampal axonal and dendritic networks (Wu and Zhang, 2016) (Figure 4G). Within the stratum radiatum of CA1, the large radial fODF lobes were parallel to the densely populated dendrites as shown on MAP2 stains (Wu and Zhang, 2016) (Figure 4G). In the stratum lacunosum moleculare of CA1, there were large tangential fODF lobes which were parallel to axons believed to be the Schaffer collaterals (Wu and Zhang, 2016) (Figure 4G). Diffusion MRI tractography within CA1 was found to closely correspond to the spatial projection pattern uncovered by tracer injection (Wu and Zhang, 2016) (Figure 4F). Using OGSE, it was found that differences in diffusivity across a range of diffusion times corresponded to apparent cell loss (H&E staining) and neurodegeneration and reactive gliosis (Fluoro-Jade C staining) within the pyramidal and granular cell layers (Aggarwal et al., 2013). Finally, a detailed biophysical model built for characterizing glia in gray matter was shown to be sensitive and specific to astrocyte and microglia alterations (Garcia-Hernandez et al., 2022). By inducing neuroinflammation without neurodegeneration, a fast microglia response was found, with increased cell body size, dispersion, and retracted cellular processes that were mirrored by the microglia parameters of the biophysical model (Garcia-Hernandez et al., 2022). As well, 24 hours after inducing neuroinflammation, the astrocytes grew in volume, a result that was also reflected in the astrocyte parameter of the model (Garcia-Hernandez et al., 2022).

Table 1. Summary of acquisitions, hardware, and diffusion models used across studies.

Authors	Key MRI parameters - Magnet Strength - Resolution - Sequence - Diffusion Sampling - TE and TR	Study Samples (N)	dMRI Model(s)	Analysis Type(s)

	- Diffusion Time			
Aggarwal et al., 2013	<ul style="list-style-type: none"> - 11.7T magnet - 0.100 mm³ resolution - DW-GRASE SE sequence - 2 b=0s/mm² and 9 directions at b=1200s/mm² and 1 b=0s/mm² and 4 directions at ~b=700s/mm² for the oscillating sequence - TE=33ms, TR=800ms and TE=50ms, TR=800ms - Δ=15ms, δ=3.2ms - For oscillating sequence, effective diffusion times = 1.67, 2.5, and 5 ms 	<u>C57BL6 mice</u> <u>ex vivo</u> <ul style="list-style-type: none"> - Hypoxia-Ischemia (15) - Healthy controls (15) 	<ul style="list-style-type: none"> - DTI - ADC - Frequency dependent ADC 	<ul style="list-style-type: none"> - Laminar (ADC) - Histology
Augustinack et al., 2010	<ul style="list-style-type: none"> - 4.7T magnet - 0.200 or 0.300 mm³ resolution - 3D SE sequence - 2 b=0s/mm² and 20 directions at b=4000s/mm² - TE=28ms, TR=250ms or TE=27.85ms, TR=320ms - Δ=10.4ms, δ=7ms 	<u>Human ex vivo</u> <ul style="list-style-type: none"> - Healthy controls (6) 	<ul style="list-style-type: none"> - DTI 	<ul style="list-style-type: none"> - Tractography - Histology
Beaujoin et al., 2018	<ul style="list-style-type: none"> - 11.7T magnet - 0.300 mm³ resolution - PGSE sequence - 96 b=0s/mm² and 500 directions at b=4500s/mm²; 60 directions at b=4500, 7500, and 10000s/mm² - TE=24.2ms, TR=9s - Δ=14.4, 30, and 45ms; δ=4.3ms 	<u>Human ex vivo</u> <ul style="list-style-type: none"> - Healthy control (1) 	<ul style="list-style-type: none"> - DTI - Q-ball - NODDI 	<ul style="list-style-type: none"> - Laminar (NDI) - Long-axis (NDI) - Tractography - Orientation distributions

Coras et al., 2014	<ul style="list-style-type: none"> - 7T magnet - 0.109 x 0.109 x 0.7 mm resolution - EPI sequence - 126 directions at $b=1200 \text{ s/mm}^2$ with 36 averages - TE=57ms, TR=9s 	<u>Human ex vivo</u> <ul style="list-style-type: none"> - Healthy controls (5) - Sclerosis (5) 	- DTI	<ul style="list-style-type: none"> - Laminar (FA, MD) - Tractography - Histology - Subfields
Garcia-Hernandez et al., 2022	<ul style="list-style-type: none"> - 7T and 3T magnet - 0.255 x 0.255 x 0.6 mm resolution; 2 mm³ resolution - EPI sequence - 4 $b=0 \text{ s/mm}^2$ and 30 directions at $b=2000$ and 4000 s/mm^2; 6 $b=0 \text{ s/mm}^2$ and 30 directions at $b=2000 \text{ s/mm}^2$ and 60 directions at $b=4000 \text{ s/mm}^2$ - TE=25ms, TR=7000ms; TE=80ms, TR=3900ms - Td=15, 25, 40, and 60ms; Td=17.3, 30, 42, and 55ms 	<u>Rat in vivo</u> <ul style="list-style-type: none"> - LPS: 8 hours (6) - LPS: 24 hours (11) - PLX5622 + LPS (7) - LPS: 15 days (5) - IBO: 14 days (9) - LYS: 14-21 days (5) * Control hippocampi were contralateral hemisphere from injection site <u>Human in vivo</u> <ul style="list-style-type: none"> - Healthy controls (6) 	- Developed biophysical model for glial cells	<ul style="list-style-type: none"> - Whole hippocampus - Histology
Jespersen et al., 2010	<ul style="list-style-type: none"> - 16.4T magnet - 0.100 mm³ resolution - SE sequence - 144 directions at 16 linearly spaced b-values from 0 to 15000 s/mm^2 - TE=14.7ms, TR=3s - $\Delta=8 \text{ ms}$, $\delta=2 \text{ ms}$ 	<u>Wistar rat ex vivo</u> <ul style="list-style-type: none"> - Healthy controls (3) 	<ul style="list-style-type: none"> - DTI - DKI - Two biophysical models 	<ul style="list-style-type: none"> - Light and electron microscopy - Model comparison - Orientation distributions

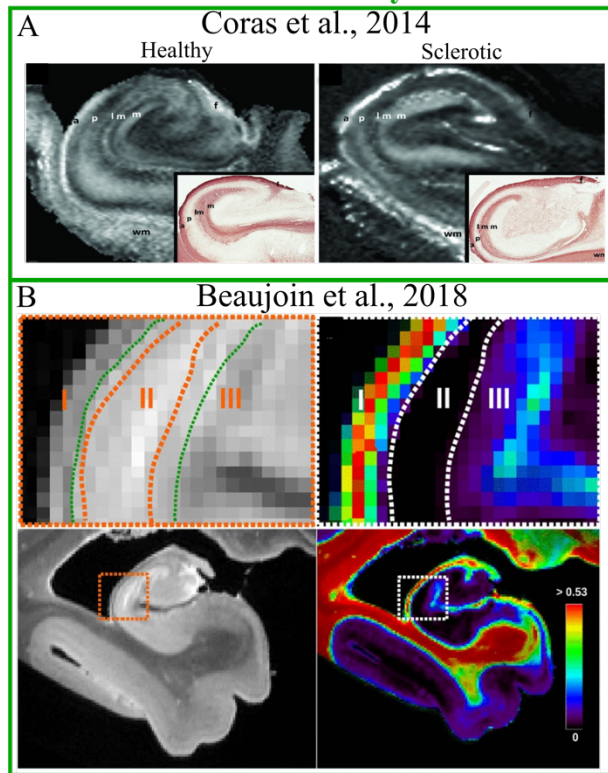
Karat et al., 2023	<ul style="list-style-type: none"> - 3T magnet - 1.25 mm³ resolution - SE-EPI sequence - 18 b=0s/mm² and 90 directions at b=1000, 2000, 3000s/mm² - TE=89.5ms, TR=5.5s 	<u>Human in vivo</u> <ul style="list-style-type: none"> - Healthy controls (100) 	<ul style="list-style-type: none"> - DTI - NODDI 	<ul style="list-style-type: none"> - Subfields - Long-axis
Khan et al., 2015	<ul style="list-style-type: none"> - 11.7T magnet - 0.250 mm³ resolution - multi-slice SE sequence - 10 b=0 s/mm² and 63 directions at b=2500 s/mm² - TE=42ms, TR=12.5s - Δ=21ms, δ=12ms 	<u>Rhesus Macaque ex vivo</u> <ul style="list-style-type: none"> - Healthy control (1) 	<ul style="list-style-type: none"> - DTI 	<ul style="list-style-type: none"> - Laminar CA1 (FA, V1) - Confocal microscopy
Ly et al., 2020	<ul style="list-style-type: none"> - 11.7T magnet - Resolution arrayed from 0.1mm³ to 0.4mm³ - 3D PGSE sequence - Diffusion directions from 12 to 256 with b-values from 1000 to 10000 s/mm² - TE=25ms, TR=1100ms - Δ=15ms, δ=4ms, Td=13.6ms 	<u>Human ex vivo</u> <ul style="list-style-type: none"> - Intractable epilepsy (3) 	<ul style="list-style-type: none"> - DTI 	<ul style="list-style-type: none"> - Laminar (FA, MD) - Tractography - Histology - Subfields
Modo et al., 2016	<ul style="list-style-type: none"> - 11.7T magnet - 0.100 mm³ resolution - 3D PGSE sequence - 1 b=0s/mm² and 6 directions at b=4000s/mm² - TE=28ms, TR=1100ms - Δ=15ms; δ=2.5, 4.0, and 6.5ms; Td=12.80, 13.60, and 14.16ms 	<u>Human ex vivo</u> <ul style="list-style-type: none"> - Intractable epilepsy (1) 	<ul style="list-style-type: none"> - DTI 	<ul style="list-style-type: none"> - Subfields - Tractography - Histology

Shepherd et al., 2006	<ul style="list-style-type: none"> - 14.1T magnet - 0.05 x 0.05 x 0.2 mm resolution - PGSE sequence - 1 $b=0\text{s/mm}^2$ and 21 directions at $\sim b=1250\text{s/mm}^2$ - TE=28.3ms, TR=1.5s - $\Delta=17.8\text{ms}$, $\delta=2.4\text{ms}$, Td=17ms 	<u>Long-Evans rat</u> <u>ex vivo</u> <ul style="list-style-type: none"> - Healthy controls (5) 	- DTI	<ul style="list-style-type: none"> - Laminar (MD, FA, V1) - Tractography - Subfields
Shepherd al., 2007	<ul style="list-style-type: none"> - 14.1T magnet - 0.06 x 0.06 x 0.3 mm resolution - Multisection PGSE sequence - 1 $b=0\text{ s/mm}^2$ with 36 averages and 21 directions at $b=1250\text{ s/mm}^2$ with 12 averages - TE=34ms, TR=1.5s - Td =17ms, $\delta=2.4\text{ms}$ 	<u>Human ex vivo</u> <ul style="list-style-type: none"> - Healthy controls (5) 	- DTI	<ul style="list-style-type: none"> - Laminar (FA, MD, V1) - Histology
Shih et al., 2023	<ul style="list-style-type: none"> - 16.4T magnet - 0.15 mm^3 resolution - 3D SE sequence - 6 $b=0\text{ s/mm}^2$ and 20, 30, and 45 directions at $b=1000, 3000, \text{ and } 5000\text{ s/mm}^2$ - TE=19ms, TR=200ms - $\Delta=10\text{ms}$, $\delta=3\text{ms}$, Td=9ms 	<u>Human ex vivo</u> <ul style="list-style-type: none"> - Healthy controls (6) - Alzheimer's Disease (4) 	<ul style="list-style-type: none"> - DTI - CSD 	<ul style="list-style-type: none"> - Laminar Dentate Gyrus (FA, MD, RD, AD) - Tractography - Histology
Stolp et al., 2018	<ul style="list-style-type: none"> - 7T magnet - 0.125 x 0.125 x 0.2 mm resolution - FSE sequence - 42 directions at $b=1500\text{s/mm}^2$, 40 averages - TE=41.30ms, TR=3600ms - $\Delta=26\text{ms}$, $\delta=5\text{ms}$ 	<u>C57Bl/6 mice</u> <u>ex vivo</u> <ul style="list-style-type: none"> - Healthy controls (9) 	<ul style="list-style-type: none"> - DTI - CSD 	<ul style="list-style-type: none"> - Laminar (MD, FA, AD, RD, AFD) - Subfields - Orientation distributions - Histology - Confocal microscopy

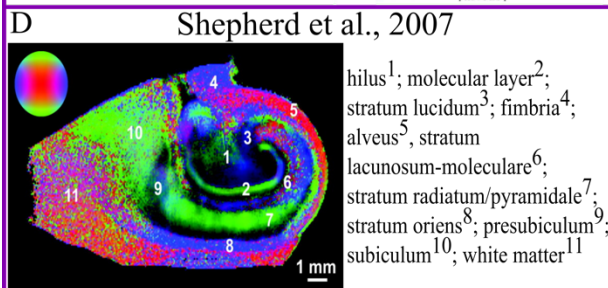
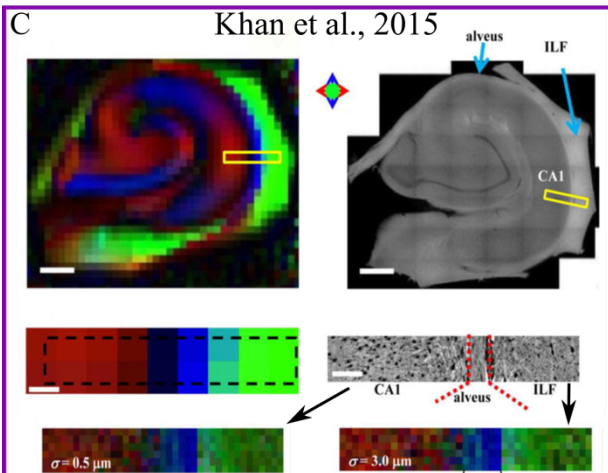
Treit et al., 2019	<ul style="list-style-type: none"> - 3T magnet - 1 mm³ resolution - Single-shot 2D EPI GRAPPA sequence (R=2) - 10 b=0s/mm² and 10 directions at b=500s/mm², 10 averages - TE=72ms, TR=2800ms 	<u>Human in vivo</u> <ul style="list-style-type: none"> - Healthy controls (19) - Temporal lobe epilepsy (18) <u>Human ex vivo</u> <ul style="list-style-type: none"> - Temporal lobe epilepsy (4) 	<ul style="list-style-type: none"> - DTI 	<ul style="list-style-type: none"> - Subfields - Long-axis - Histology
Wu et al., 2018	<ul style="list-style-type: none"> - 11.7T magnet - 0.17 x 0.17 x 0.8 mm resolution - 4-segment multi-slice EPI - 30 directions at b=1000s/mm² and b=2000s/mm² - TE=55ms, TR=3000ms - Δ=20ms, δ=4ms - For oscillating sequence, effective diffusion time = 2.5 ms 	<u>C57BL6 mice ex vivo</u> <ul style="list-style-type: none"> - Hypoxia-Ischemia (5) - Healthy controls (6) 	<ul style="list-style-type: none"> - DTI - DKI 	<ul style="list-style-type: none"> - Whole hippocampus - Subfields - Long-axis - Histology
Wu and Zhang, 2016	<ul style="list-style-type: none"> - 11.7T magnet - 0.100 mm³ resolution - 3D DW-GRASE sequence - 4 b=0s/mm² and 30 or 60 directions at b=2500s/mm² - TE=21ms, TR=500ms - Δ=12ms, δ=4ms 	<u>C57BL/6 mice in vivo</u> <ul style="list-style-type: none"> - Healthy controls (12) 	<ul style="list-style-type: none"> - DTI - CSD 	<ul style="list-style-type: none"> - Laminar (MD, FA) - Tractography - Subfields - Registration to Allen Reference Atlas (Tract tracing and histology)
Yoo et al., 2021	<ul style="list-style-type: none"> - 3T magnet - 1.5 mm³ resolution - EPI sequence with linear and spherical b-tensor encoding - 41 b=0s/mm² and 12 directions at b=200, 750, 1000, 1250s/mm² and 32 directions at b=1500, 1750, and 2000s/mm² - TE=101ms, TR=4.6s 	<u>Human in vivo</u> <ul style="list-style-type: none"> - Healthy controls (8) 	<ul style="list-style-type: none"> - DTI - Microscopic FA 	<ul style="list-style-type: none"> - Whole hippocampus - Long-axis

Zeineh et al., 2012	<ul style="list-style-type: none"> - 3T magnet - 1.4 mm³ resolution - EPI GRAPPA accelerated sequence (R=2) - 10 b=0s/mm² and 70 directions at b=1500s/mm² - TE=69ms, TR=3150ms 	<u>Human in vivo</u> - Healthy controls (6)	- DTI	<ul style="list-style-type: none"> - Subfields - Tractography
---------------------	---	--	-------	---

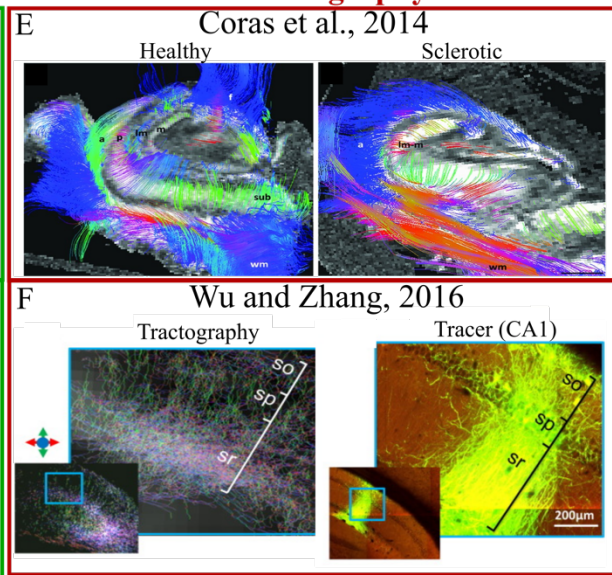
Laminar Analyses



Diffusion Orientations



Tractography



Histology

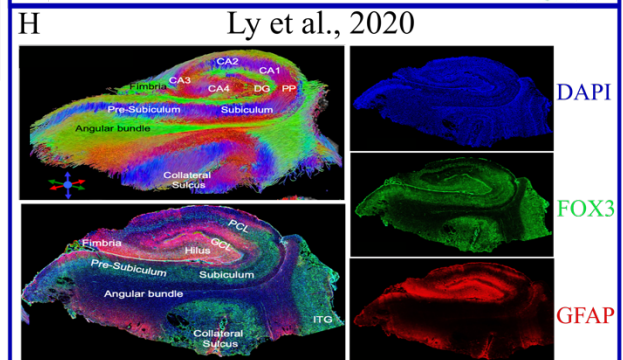
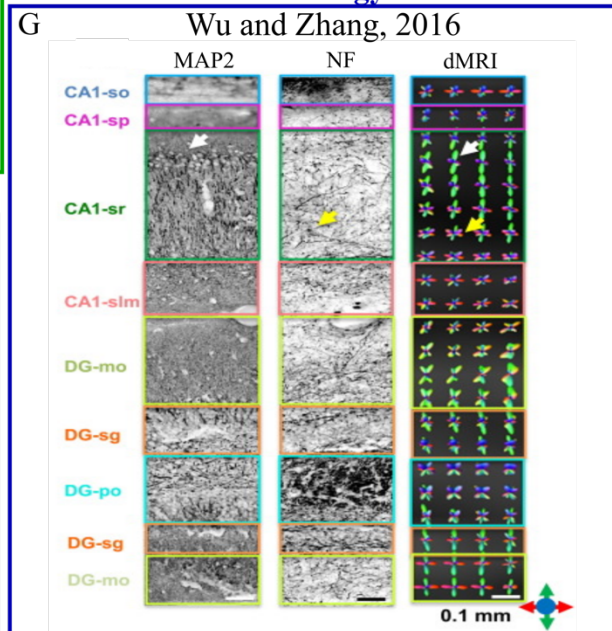


Figure 4. Illustration of hippocampal dMRI results based on some of the categories defined in the right column of Table 1 (i.e., Analysis types). For a brief summary of the presented results see the below section (Summary of key findings). (A) Adapted from Coras et al., 2014 with permission. Left panel represents a healthy control and the right panel represents a sclerotic hippocampus. Grey-scaled images represent FA maps. Insets represent histological slices stained for myelin basic protein. (B) Adapted from Beaujoin et al., 2018 with permission. Top left depicts a T2w image with the zoom shown in the bottom left figure. I (alveus, str. oriens), II (str. pyramidale), and III (str. lucidum radiatum lacunosum moleculare) correspond to the three laminar layers of the hippocampus. Top right represents the intracellular-volume fraction map obtained with the NODDI model. (C) Adapted from Khan et al., 2015 with permission. Coronal sections of a rhesus macaque hippocampus. Top left is the primary eigenvector map (V1) derived from DTI and scaled by FA. Top right is a 200 μ m thick tissue obtained at 10x magnification using 3D confocal microscopy. Bottom left is a zoomed in depiction of the DTI color map depicted in the top left. Bottom right depicts one slice of the 3D confocal microscopy acquired at 63x magnification and digitized at 0.25 μ m resolution. Arrows depict the 3D structure tensor analysis using kernel sizes of 0.5 μ m and 3.0 μ m to define the local region used for computing spatial derivatives. (D) Adapted from Shepherd et al., 2007 with permission. Coloured image is the FA-scaled primary eigenvector (V1) with transverse (blue), vertical (green) or through-plane (red) orientations. (E) Adapted from Coras et al., 2014 with permission. Left column represents a healthy control and the right column represents a sclerotic hippocampus. Coloured image represents DTI tractography. (F) Adapted from Wu et al., 2016 with permission. Left figure is laminar tractography in CA1. Right figure is a similar slice with AAV tracer acquired using serial two-photon microscopy. (G) Adapted from Wu et al., 2016 with permission. Left column

shows stained coronal sections of MAP2 (dendrites and cell bodies) while the middle column shows similar slices of NF (axons) across the laminae in CA1 and the dentate gyrus. The far-right column represents the Fiber Orientation Distribution (fODF) maps derived from dMRI. (H) Adapted from Ly et al., 2020 with permission. Top left represents a coronal slice of tractography from a human hippocampus. Bottom left represents combined immunohistochemistry seen on the right side of the same coronal slice. Right column represents immunohistochemical staining of DAPI (general cellularity), FOX3 (neurons) and GFAP (glial cells).

Summary of key findings

Here we present a brief bullet-point list that synthesizes some of the key results reviewed in the previous sections and are illustrated in Figure 4.

- At high resolutions, DTI metrics of FA and MD appear to be sensitive but not specific to the microstructural properties of the hippocampal laminae, from highly myelinated regions to the neuropil and perikarya (Coras et al., 2014) (Figure 4A). This outcome has been corroborated by many studies applying DTI in health and a variety of diseased states both *in vivo* and *ex vivo*, suggesting that these DTI metrics may reflect a mixture of multiple microstructural barriers that hinder water movement (Coras et al., 2014; Jespersen et al., 2010; Shepherd et al., 2006, 2007; Stolp et al., 2018; Yoo et al., 2021).
- Biophysical modeling provides a promising avenue for providing more complete descriptions of the hippocampal microstructure, including laminar and long-axis differentiation (Beaujoin et al., 2018) (Figure 4B), identification of myelinated fiber tracts, such as the perforant path, and the documentation of abundant glial cells (Garcia-Hernandez et al., 2022; Jespersen et al., 2010; Karat et al., 2023; Tournier et al., 2007).

- Acquisitions utilizing ultra-short diffusion times have shown unique laminar-specific properties and significant changes in diseased states, which can likely be attributed to varying sensitivity of the measured signal to microstructure existing on various spatial scales (Aggarwal et al., 2013; Wu et al., 2018).
- Microscopic anisotropy was found to be much larger than fractional anisotropy (ensemble anisotropy) in the whole hippocampus, suggesting there is a lot of orientation dispersion (Yoo et al., 2021).
- Capitalizing on the angular richness of the dMRI signal, distinct microstructural orientations have been found throughout the hippocampus, allowing for improved delineation of internal hippocampal circuitry (Beaujoin et al., 2018; Jespersen et al., 2010; Karat et al., 2023; Khan et al., 2015; Laitinen et al., 2010; Ly et al., 2020; Shepherd et al., 2006, 2007; Sierra et al., 2015; Tuch, 2008; Wu and Zhang, 2016). (Figure 4C, D, and H). Leveraging these orientations for tractography has proven useful to capture hippocampal circuitry in-vivo at high spatial-resolution and uncover orientation shifts reflecting abnormalities in diseased states (Augustinack et al., 2010; Beaujoin et al., 2018; Ly et al., 2020; Modo et al., 2015; Shepherd et al., 2006; Zeineh et al., 2012) (Figure 4E and H). Comparing dMRI orientation models to histology has suggested that the basic organization of hippocampal axonal and dendritic networks and their properties, such as the Schaffer collaterals can be captured (Wu and Zhang, 2016) (Figure 4G).

Concluding remarks and future directions

Diffusion MRI offers a promising avenue for characterizing microstructure of the hippocampus and its intrinsic circuitry. Importantly, hippocampal microstructure is known to

deteriorate as a consequence of a wide range of diseases, with significant consequences for cognitive functioning, making dMRI an attractive method for exploration of earlier and more accurate disease characterization (Small et al., 2011). While promising, modeling the dMRI signal within the hippocampal gray matter is an arduous task owing to its heterogeneous microstructure. Challenges include the presence of large soma and potential water exchange from the intra- to extracellular space. Greatly increasing the complexity of this problem is the breadth of diffusion acquisitions used across studies, including variation in diffusion sensitization (i.e., gradient strength and length) and diffusion times. In the studies reviewed here, reported diffusion times typically ranged from 2.5 to 60 ms (Table 1), which probe contrasting micro-scale diffusion displacements. This variation makes a synthesis of results difficult. Thus, in future studies it is pertinent that diffusion times be reported in conjunction with the b-value (or gradient strength and length). Relatedly, it is clear that the interpretation of dMRI metrics is enhanced with an anatomically grounded approach, where the microstructure in the region of interest is well considered. For example, by relating dMRI metrics to known layer specific changes in cyto- and myeloarchitecture, or by linking diffusion orientations to histologically derived microstructural orientations (Coras et al., 2014; Shepherd et al., 2006, 2007; Stolp et al., 2018). However, the ability to take an anatomically grounded approach is limited by resolution, given that the hippocampus is a relatively thin structure (laminar thickness of ~0.5-3mm) and partial voluming across many disparate microstructural compartments is abundant. Finally, new open datasets combining microscopy, *ex vivo* and *in vivo* MRI such as BigMac (Howard et al., 2023) have great promise in improving the link between the diffusion MRI signal and the known hippocampal microstructure. The current state of the field encourages pursuit of important and exciting avenues for future dMRI research on the hippocampus.

Outstanding questions

Here we highlight some outstanding and interesting questions that arose as a result of the synthesis of the reviewed studies.

- Can biophysical models specifically developed for gray matter (which incorporate water exchange and/or a soma compartment) improve specificity to hippocampal microstructure?
- To what degree is the hippocampal microstructure oriented radially and tangentially? Can dMRI metrics be related to specific hippocampal microstructure based on previous knowledge of their orientations? Finally, to what extent do hippocampal microstructural orientations vary across individuals and can distinct changes in microstructural orientations be discerned in diseased states?
- As MRI hardware improves and stronger gradients become increasingly available, shorter diffusion length scales can be probed. Can diffusion time be leveraged to capture particular aspects of hippocampal microstructure that exist at various spatial scales?
- Is tract-tracing a viable method for validating the sensitivity of diffusion tractography to hippocampal circuitry?
- To what degree are the conclusions drawn from hippocampal dMRI affected by resolution? At what resolution does extra-hippocampal myelinated microstructure dominate the dMRI signal?
- Are there consistent hippocampal long-axis (anterior-posterior) differences in the dMRI signal across different models?
- Does microscopic fraction anisotropy (uFA) provide contrast to the laminae and subfields?

- Does hippocampal uFA have a dominant histological correlation?
- Particular regions of the hippocampus were found to have unique cellular compositions.
For example, the subiculum and CA1 were shown to have lower amounts of glial cells.
Can a spatially-adaptive hippocampal dMRI model improve microstructural specificity by taking advantage of known microstructural compositions?
- What are the relationships between microstructural properties revealed with higher-order dMRI modeling and specific cognitive processes known to be supported by the hippocampus? How are these relationships altered by disease states that affect hippocampal integrity?

References

- Afzali M, Mueller L, Szczepankiewicz F, Jones DK, Schneider JE (2022) Quantification of tissue microstructure using tensor-valued diffusion encoding: brain and body. *Front Phys* 10.
- Aggarwal M, Burnsed J, Martin LJ, Northington FJ, Zhang J (2013) Imaging neurodegeneration in the mouse hippocampus after neonatal hypoxia-ischemia using oscillating gradient diffusion MRI. *Magn Reson Med* 72:829–840.
- Amaral D, Lavenex P (2007) Hippocampal Neuroanatomy. In: *The hippocampus book* (Andersen P, Morris R, Amaral D, Bliss T, O’Keefe J, eds), pp37-110. New York: Oxford UP.
- Augustinack JC, Helmer K, Huber KE, Kakunoori S, Zöllei L, Fischl B (2010) Direct visualization of the perforant pathway in the human brain with ex vivo diffusion tensor imaging. *Front Hum Neurosci* 4.
- Basser PJ, Mattiello J, LeBihan D (1994) MR diffusion tensor spectroscopy and imaging. *Biophys J* 66:259–267.
- Beaujoin J, Palomero-Gallagher N, Boumezbeur F, Axer M, Bernard J, Poupon F, Schmitz D, Mangin JF, Poupon C (2018) Post-mortem inference of the human hippocampal connectivity and microstructure using ultra-high field diffusion MRI at 11.7 T. *Brain Struct Funct* 223:2157–2179.
- Brown R (1828) A brief account of microscopical observations made in the months of June, July and August 1827, on the particles contained in the pollen of plants; and on the general existence of active molecules in organic and inorganic bodies. *Philos Mag* 4:161–173.
- Coras R, Milesi G, Zucca I, Mastropietro A, Scotti A, Figini M, Mühlebner A, Hess A, Graf

- W, Tringali G, Blümcke I, Villani F, Didato G, Frassoni C, Spreafico R, Garbelli R (2014) 7T MRI features in control human hippocampus and hippocampal sclerosis: An ex vivo study with histologic correlations. *Epilepsia* 55:2003–2016.
- Descoteaux M, Angelino E, Fitzgibbons S, Deriche R (2007) Regularized, fast, and Robust Analytical q-ball imaging. *Magn Reson Med* 58:497–510.
- Ding S, Van Hoesen GW (2015) Organization and detailed parcellation of human hippocampal head and body regions based on a combined analysis of cyto- and chemoarchitecture. *J Comp Neurol* 523: 2233–2253.
- Duvernoy HM (2005) Structure, Functions, and Connections. In: *The Human Hippocampus*, pp5-37. Berlin, Heidelberg: Springer.
- Fellgiebel A, Yakushev I (2011) Diffusion Tensor Imaging of the Hippocampus in MCI and Early Alzheimer’s Disease. *J Alzheimer’s Dis* 26:257–262.
- Garcia-Hernandez R, Cerdá CA, Carpena AT, Drakesmith M, Koller K, Jones DK, Canals S, De Santis S (2022) Mapping microglia and astrocyte activation in vivo using diffusion MRI. *Sci Adv* 8.
- Grussu F, Schneider T, Tur C, Yates RL, Tachrount M, Ianaş A, Yiannakas MC, Newcombe J, Zhang H, Alexander DC, DeLuca GC, Gandini Wheeler-Kingshott CA (2017) Neurite dispersion: A new marker of multiple sclerosis spinal cord pathology? *Ann Clin Transl Neurol* 4:663–679.
- Howard AFD, Huszar IN, Smart A, Cottaar M, Daubney G, Hanayik T, Khrapitchev AA, Mars RB, Mollink J, Scott C, Sibson NR, Sallet J, Jbabdi S, Miller KL (2023) An open resource combining multi-contrast MRI and microscopy in the macaque brain. *Nat Commun* 14.

- Insausti R, Amaral D (2004) Hippocampal formation. In The human nervous system, 2nd Edn (Paxinos G, Mai JK, eds), pp871-914. Cambridge MA: Academic Press.
- Jelescu IO, Budde MD (2017) Design and Validation of Diffusion MRI Models of White Matter. *Front Phys* 5.
- Jelescu IO, Palombo M, Bagnato F, Schilling KG (2020) Challenges for biophysical modeling of Microstructure. *J Neurosci Methods* 344.
- Jelescu IO, de Skowronski A, Palombo M, Novikov DS (2022) Neurite Exchange Imaging (NEXI): A minimal model of diffusion in gray matter with inter-compartment water exchange. *NeuroImage* 256:119277–119277.
- Jensen JH, Helpern, JA (2010) MRI quantification of non-gaussian water diffusion by kurtosis analysis. *NMR Biomed* 23:698–710.
- Jensen JH, Helpern JA, Ramani A, Lu H, Kaczynski K (2005) Diffusional kurtosis imaging: The quantification of non-gaussian water diffusion by means of magnetic resonance imaging. *Magn Reson Med* 53:1432–1440.
- Jespersen SN, Carsten RB, Jens RN, Chakravarty MM, Hansen B, Vosegaard T, Østergaard L, Yablonskiy D, Nielsen N, Vestergaard-Poulsen P (2010) Neurite Density from Magnetic Resonance Diffusion Measurements at Ultrahigh Field: Comparison with Light Microscopy and Electron Microscopy. *NeuroImage* 49:205–16.
- Jones DK, Leemans A (2010) Diffusion tensor imaging. In: Magnetic resonance neuroimaging (Modo M, Bulte J, eds), pp127-144. Humana press.
- Jones DK (2011) Diffusion MRI: theory, methods, and applications. New York: Oxford University Press.
- Jung BA, Weigel M (2013) Spin Echo Magnetic Resonance Imaging. *J Magn Reson Imaging* 37:

805–817.

Karat BG, DeKraker J, Hussain U, Köhler S, Khan AR (2023) Mapping the Macrostructure and Microstructure of the in Vivo Human Hippocampus Using Diffusion MRI. *Hum Brain Mapp.*

Khan AR, Cornea A, Leigland LA, Kohama SG, Jespersen SN, Kroenke CD (2015) 3D structure tensor analysis of light microscopy data for validating diffusion MRI. *NeuroImage* 111:192–203.

Koh DM, Collins DJ (2007) Diffusion-weighted MRI in the body: Applications and challenges in oncology. *Am J Roentgenol* 188: 1622–1635.

Laitinen T, Sierra A, Pitkänen A, Gröhn O (2010) Diffusion tensor MRI of axonal plasticity in the rat hippocampus. *NeuroImage* 51:521–530.

Le Bihan (2010) Magnetic Resonance Diffusion Imaging: Introduction and Concepts. In *Diffusion MRI: Theory, Methods, and Applications* (Jones DK, ed), pp57-78. New York: Oxford University Press.

Le Bihan D, Iima M (2015). Diffusion magnetic resonance imaging: What water tells us about biological tissues. *PLoS Biol* 13.

Ly M, Foley L, Manivannan A, Hitchens TK, Richardson RM, Modo M (2020) Mesoscale diffusion magnetic resonance imaging of the ex vivo human hippocampus. *Hum Brain Mapp* 41:4200–4218.

McRobbie D, Moore E, Graves M, Prince M (2017) What You Set is What You Get: Basic Image Optimization. In: *MRI from Picture to Proton*, pp. 67-80. Cambridge: Cambridge University Press.

Modo M, Hitchens TK, Liu JR, Richardson RM (2015) Detection of aberrant hippocampal

- mossy fiber connections: Ex vivo mesoscale diffusion MRI and microtractography with histological validation in a patient with uncontrolled temporal lobe epilepsy. *Hum Brain Mapp* 37:780–795.
- Mori S, Zhang J (2006) Principles of diffusion tensor imaging and its applications to basic neuroscience research. *Neuron* 51:527–539.
- Nieuwenhuys R, Voogd J, Van Huijzen C (2008) Telencephalon: Hippocampus and Related Structures. In: *The Human Central Nervous System*, pp361-386. Berlin, Heidelberg: Springer.
- Novikov DS, Fieremans E, Jespersen SN, Kiselev VG (2018) Quantifying brain microstructure with diffusion MRI: Theory and parameter estimation. *NMR Biomed* 32.
- Palombo M, Ianus A, Guerreri M, Nunes D, Alexander DC, Shemesh N, Zhang H (2020) SANDI: A compartment-based model for non-invasive apparent soma and neurite imaging by diffusion MRI. *NeuroImage* 215:116835–116835.
- Qian W, Khattar N, Cortina LE, Spencer RG, Bouhrara M (2020) Nonlinear associations of neurite density and myelin content with age revealed using multicomponent diffusion and relaxometry magnetic resonance imaging. *NeuroImage* 223: 117369.
- Rosene DL, Van Hoesen GW (1987) The hippocampal formation of the primate brain. In: *Cerebral cortex: Further aspects of cortical function, including hippocampus* (Jones EG, Peters A, eds), pp345-456. New York: Plenum Press.
- Saunders RC, Aggleton JP (2007) Origin and topography of fibers contributing to the fornix in Macaque Monkeys. *Hippocampus* 17:396–411.
- Schilling KG, Janve V, Gao Y, Stepniewska I, Landman BA, Anderson AW (2018) Histological

- validation of diffusion MRI fiber orientation distributions and dispersion. *NeuroImage* 165:200–221.
- Sepehrband F, Clark KA, Ullmann JFP, Kurniawan ND, Leanage G, Reutens DC, Yang Z (2015) Brain tissue compartment density estimated using diffusion-weighted MRI yields tissue parameters consistent with histology. *Hum Brain Mapp* 36:3687–3702.
- Shepherd TM, Özarlan E, King MA, Mareci TH, Blackband SJ (2006) Structural insights from high-resolution diffusion tensor imaging and tractography of the isolated rat hippocampus. *NeuroImage* 32:1499–1509.
- Shepherd TM, Özarlan E, Yachnis AT, King MA, Blackband SJ (2007) Diffusion Tensor microscopy indicates the cytoarchitectural basis for diffusion anisotropy in the human hippocampus. *Am J Neuroradiol* 28:958–964.
- Shih NC, Kurniawan ND, Cabeen RP, Korobkova L, Wong E, Chui HC, Clark KA, Miller CA, Hawes D, Jones KT, Sepehrband F (2023) Microstructural Mapping of Dentate Gyrus Pathology in Alzheimer’s Disease: A 16.4 Tesla MRI Study. *NeuroImage Clin* 37:103318.
- Sierra A, Gröhn O, Pitkänen A (2015) Imaging microstructural damage and plasticity in the hippocampus during epileptogenesis. *Neurosci J* 309:162–172.
- Small SA, Schobel SA, Buxton RB, Witter MP, Barnes CA (2011) A pathophysiological framework of hippocampal dysfunction in ageing and disease. *Nat Rev Neurosci* 12:585–601.
- Stolp HB, Ball G, So PW, Tournier JD, Jones MM, Thornton C, Edwards DA (2018) Voxel-wise comparisons of cellular microstructure and diffusion-MRI in mouse hippocampus using 3D Bridging of Optically-clear histology with Neuroimaging Data (3D-BOND). *Sci Rep* 8.

- Tournier DJ, Calamante F, Connelly A (2007) Robust determination of the fibre orientation distribution in diffusion MRI: Non-negativity constrained super-resolved spherical deconvolution. *NeuroImage* 35:1459–1472.
- Treit S, Little G, Steve TA, Nowacki T, Schmitt L, Wheatley MB, Beaulieu C, Gross D (2019) Regional hippocampal diffusion abnormalities associated with subfield-specific pathology in temporal lobe epilepsy. *Epilepsia open* 4:544–554.
- Tuch DS (2004) Q-ball imaging. *Magn Reson Med* 52:1358–1372.
- Voss JL, Bridge DJ, Cohen NJ, Walker JA (2017) A Closer Look at the Hippocampus and Memory. *Trends Cogn Sci* 21:577–588.
- Williams EM, Rosenblum EW, Pihlstrom N, Llamas-Rodríguez J, Champion S, Frosch MP, Augustinack JC (2023) Pentad: A reproducible cytoarchitectonic protocol and its application to parcellation of the human hippocampus. *Front Neuroanat* 17.
- Wu D, Li Q, Northington FJ, Zhang J (2018) Oscillating gradient diffusion kurtosis imaging of normal and injured mouse brains. *NMR Biomed* 31:e3917.
- Wu D, Zhang J (2016) In vivo mapping of macroscopic neuronal projections in the mouse hippocampus using high-resolution diffusion MRI. *NeuroImage* 125:84–93.
- Yoo J, Kerkelä L, Hales PW, Seunarine KK, Clark CA (2021) High-resolution microscopic diffusion anisotropy imaging in the human hippocampus at 3T. *Magn Reson Med* 87:1903–1913.
- Zeineh MM, Holdsworth S, Skare S, Atlas SW, Bammer R (2012) Ultra-high resolution diffusion tensor imaging of the microscopic pathways of the medial temporal lobe. *NeuroImage* 62:2065–2082.
- Zeineh MM, Palomero-Gallagher N, Axer M, Gräßel D, Goubran M, Wree A, Woods RP,

Amunts K, Zilles K (2017) Direct Visualization and Mapping of the Spatial Course of Fiber Tracts at Microscopic Resolution in the Human Hippocampus. *Cereb Cortex* 27:1779-1794.

Zhang H, Schneider T, Wheeler-Kingshott CA, Alexander DC (2012) NODDI: Practical in vivo neurite orientation dispersion and density imaging of the human brain. *NeuroImage* 61:1000–1016.